Supplementary Information

External Chirality-Driven Interfacial Spin Filtering in Magnetically Aligned NiFe-LDH Facilitates the Enhancement of Oxygen Evolution Reaction

Utkarsh Utkarsh, Dibyendu Barik, Anujit Balo, Sachidananda Sahu, Koyel Banerjee Ghosh*

Department of Chemistry, Indian Institute of Technology Hyderabad, Telangana 502284, India

AUTHOR INFORMATION

Corresponding Author

Koyel Banerjee Ghosh

Department of Chemistry, Indian Institute of Technology Hyderabad, Telangana 502284, India

Email: koyel@chy.iith.ac.in

Materials

Nickel nitrate [$Ni(NO_3)_2 \cdot 6H_2O$, ≥97 %, Sigma-Aldrich], iron nitrate [$Fe(NO_3)_3 \cdot 9H_2O$, ≥98 %, Sigma-Aldrich], triethanolamine (TEA, ≥98 %, SRL), urea (99.5 %, SRL), R- and S-camphorsulfonic acid (TCI), ethanol (99.9 %, Northman), potassium hydroxide pellete (KOH, 85 %, SRL), sodium sulfate (Na_2SO_4, ≥99 %, Sigma-Aldrich), o-tolidine (98%, SRL), Poly(methylmethacrylate) (PMMA, Sigma-Aldrich), Lithium perchlorate ($LiClO_4$, ≥95 %, Sigma-Aldrich), Propylene carbonate (≥99 %, SRL), Milli-Q water, fluorine-doped tin oxide coated glass slide (FTO, resistance ~14 Ω, Sigma-Aldrich), permanent magnet.

Experimental

Synthesis of NiFe-LDH

NiFe-LDH was synthesized by following the reported protocols.[1] Briefly, the synthesis was done using the hydrothermal technique. In this procedure, nickel nitrate [15 mmol, $Ni(NO_3)_2 \cdot 6H_2O$] and iron nitrate [5 mmol, $Fe(NO_3)_3 \cdot 9H_2O$] were dissolved with triethanolamine (12.5 mmol, TEA) in 200 ml of Milli-Q water. Then, the urea solution (7 mmol, dissolved in 200 ml of water) was added while stirring. The resulting solution was transferred into a Teflon-lined autoclave and heated at 150 °C for two days in an oven. After cooling to room temperature, a yellowish powder was collected by centrifugation, washed with ethanol, and dried in a vacuum desiccator.

Fabrication of the electrode

The spin-coating method was used to fabricate the electrode on an FTO-coated glass slide. Firstly, 10 mg of catalyst in 0.5 ml of ethanol was sonicated for 15 min to prepare a homogeneous catalyst dispersion. Then, 50 µl of catalyst dispersion was spin-coated on the FTO slide and dried in a vacuum desiccator. For the chiral modification, 50 µl of camphorsulfonic acid solution in water (10 mM) was spin-coated on top of the catalyst-coated FTO slide.

Preparation of gel electrolyte

Gel electrolyte was prepared using the reported method.[2] In a typical procedure, $LiClO_4$ was heated at 100 °C for 24 h. Subsequently, 210 mg of PMMA and 90 mg of dried $LiClO_4$ were placed in a round-bottom flask, followed by the addition of 0.6 ml of propylene carbonate. Thereafter, 1 ml

of acetonitrile was added under continuous stirring. This was stirred in a nitrogen atmosphere for 24 h until a homogeneous mixture of gel electrolyte was formed.

Electrochemical study

The electrochemical behavior of the fabricated electrode was studied by using the electrochemical workstation (Biologic SP-300). A three-electrode electrochemical cell consisting of a Pt wire as a counter-electrode, Hg/HgO (filled with 1 M KOH) as a reference electrode, and a catalyst-coated FTO slide as the working electrode was used, while 1 M KOH was used as the electrolyte solution. The linear sweep voltammetry (LSV) experiment was carried out in 1 M KOH at a scan rate of 5 mV s^{-1} in the potential range of 0 to 1.2 V vs Hg/HgO. All the potential is converted with respect to the reversible hydrogen electrode (RHE) using the following equation:

$$E_{RHE} = E^{o}_{Hg/HgO} + 0.059pH + 0.098$$

Electrochemically active surface area (ECSA) of all the electrodes has been calculated in a 1 M KOH solution using the following formula:

$$ECSA = \frac{C_{dl}}{C_s}$$

Where C_{dl} and C_s are the double-layer capacitance and specific capacitance, respectively.

Characterzation

The synthesized catalyst was characterized employing X-ray diffraction (XRD) by Malvern PANalytical Empyrean using Cu Kα (1.54 Å) as an X-ray source operating at 40 kV and 40 mA. The data was recorded from 5° to 30° to reveal the crystal structure of the catalyst. X-ray photoelectron spectroscopy (XPS) was adapted for the assignment of the oxidation state and the bonding nature of the metal ions in the catalyst film. The study was carried out employing the AXIS SUPRA system using a monochromatic Al X-ray source, which has a 1486.69 eV photon energy. Scanning electron microscopy (JEOL JIB-4700F) operated with an accelerating voltage of 15 kV) was used to evaluate the microstructure and thickness of the catalyst. Fourier transform infrared (FT-IR) spectra of the thin film were measured using a Bruker Alpha-P spectrometer with 4 cm^{-1} resolution and 4000–500 cm^{-1} scan range to evaluate the chemical environment, i.e., the functional groups in the catalyst. The catalyst was also characterized by employing Raman

spectroscopy (Witec Alpha 300R) at an excitation wavelength of 532 nm. Device data (I-V response) was measured using Autolab.

DC conductance measurement in two-terminal devices

The overall conductivity in the device primarily arises from ionic conduction, where lithium ions dissociated from $LiClO_4$ serve as the main charge carriers. The high-dielectric solvents, propylene carbonate and acetonitrile, facilitate this salt dissociation and decrease the viscosity of the gel, enhancing ionic mobility.[3] PMMA acts as a polymer matrix that provides mechanical stability, while being plasticized by propylene carbonate, which lowers the polymer's glass transition temperature (T_g) and increases segmental chain mobility.[4] Electron conduction is less due to PMMA's wide bandgap (~ 4 eV) insulating nature.[5] However, we see a slight increase in conductivity going towards a mid to higher potential region, which can be attributed to the EDLC charging occurring at the interface between the electrode and electrolyte of the catalyst/FTO electrode. The low absolute current (~ µA range) is consistent with limited ionic conductivity in PMMA–$LiClO_4$ systems (10^{-5}-10^{-4} S cm^{-1}), indicating that the dominant charge transfer mechanism is field-induced ion migration rather than redox-driven conduction.[6]

VSM measurement of the catalyst (as a thin film) before and after OER:

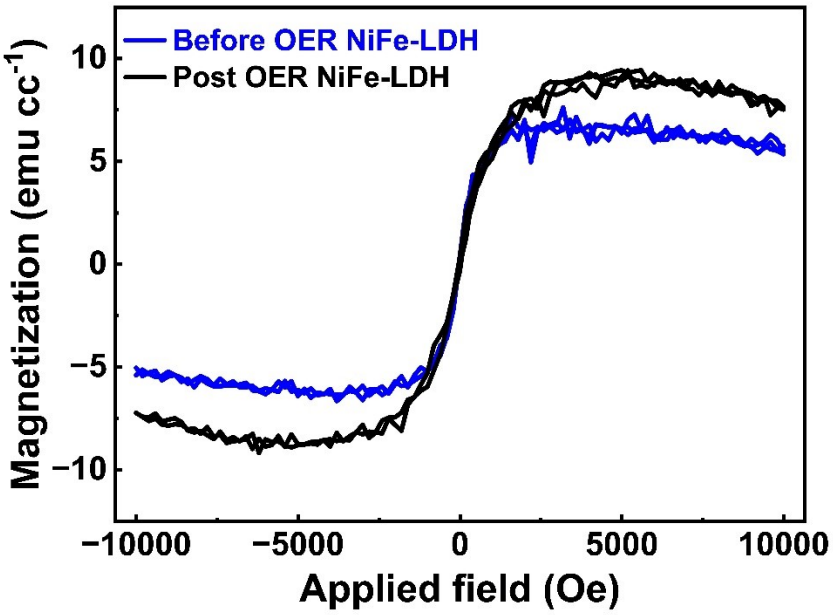

Figure S1. VSM measurement of the catalyst (as a thin film) at room temperature before and after OER.

Cross-sectional image of catalyst coated on FTO slide:

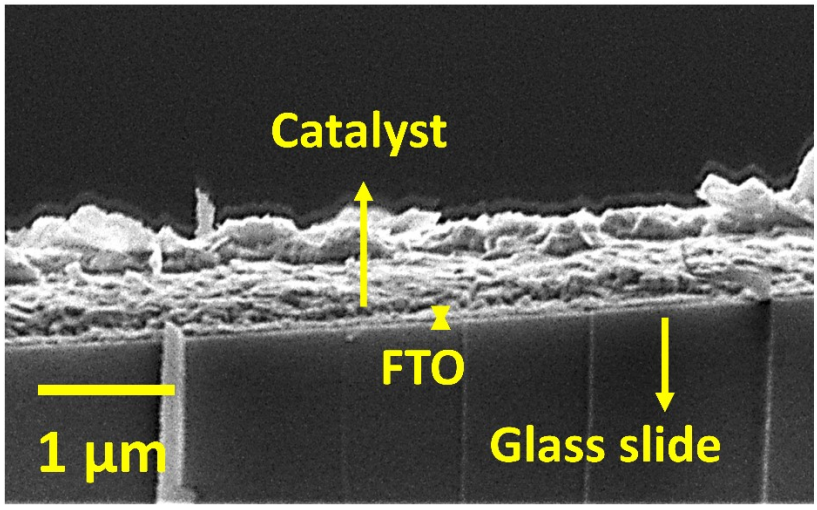

Figure S2. Cross-section image of catalyst coated on FTO slide using scanning electron microscopy.

Double-layer capacitance (C_{dl}):

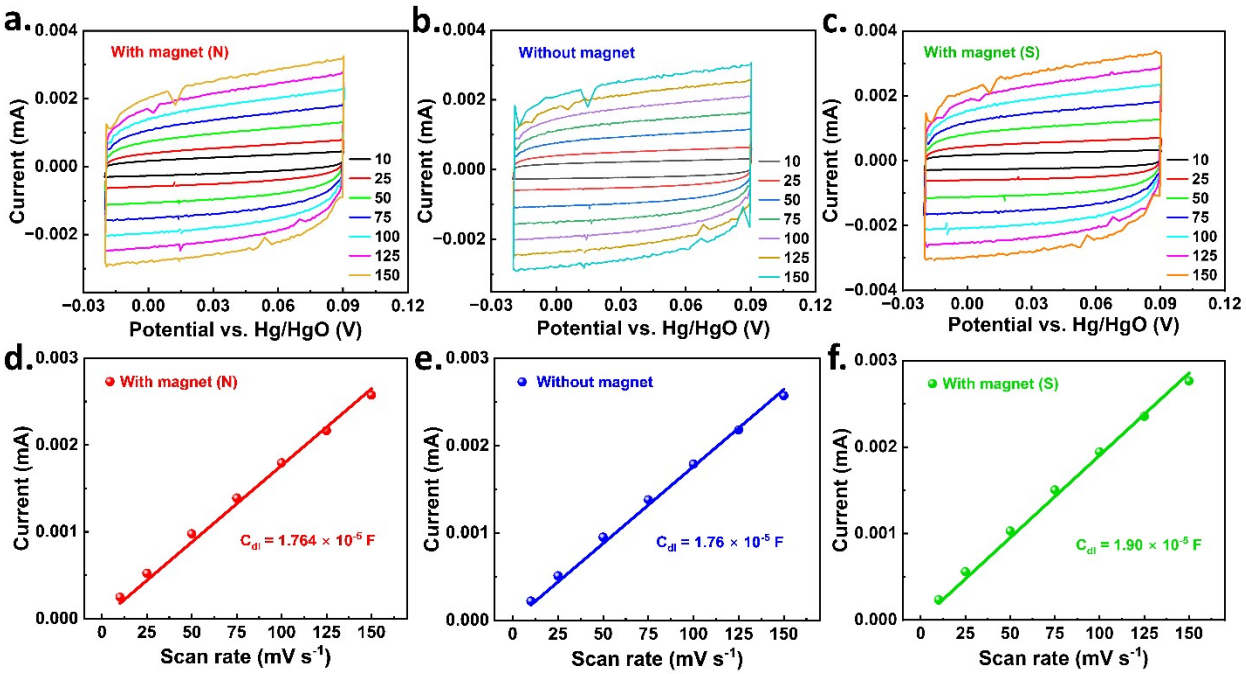

Figure S3. CV plots with different scan rates (10–150 mV s^{-1}) and plots of the average current at 0 V (vs. Hg/HgO) vs. scan rates of catalyst (a, d) with magnet (N), (b, e) without magnet, and (c, f) with magnet (S).

Current density vs. applied potential showing three independent measurements for each type of electrode:

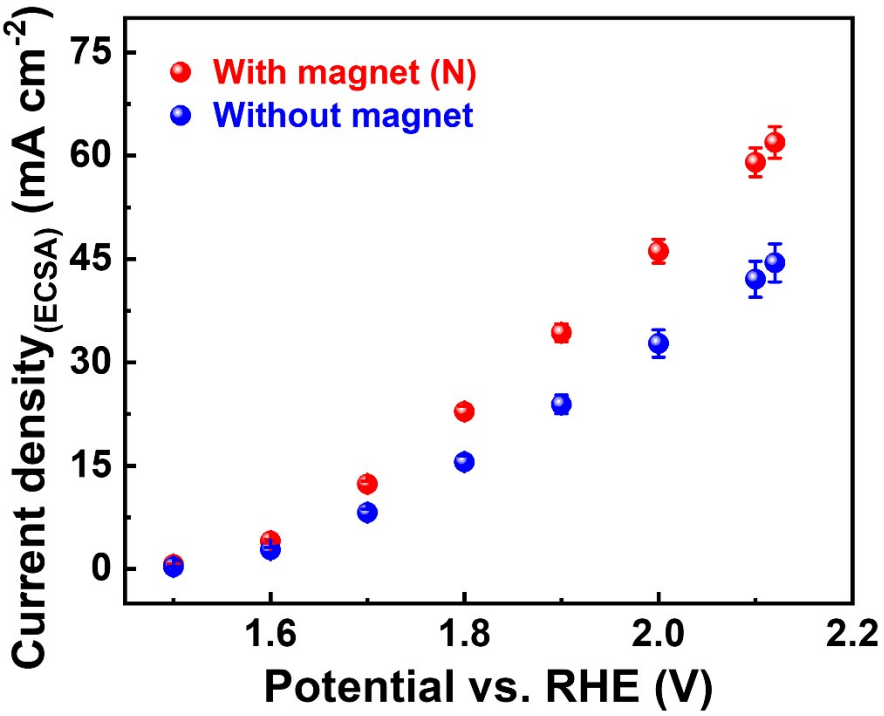

Figure S4. Current density vs. applied potential in the form of an error bar in 1 M KOH at a scan rate of 5 mV s^{-1}. Current density is normalized with electrochemically active surface area (ECSA).

Estimation of Hydrogen Peroxide Formation

To investigate the generation of hydrogen peroxide as a byproduct from different types of electrodes, electrochemical experiments were performed in neutral media (pH 6.5) using 0.1 M Na_2SO_4 electrolyte solution. LSV plots displayed in **Figure S5a** show that the catalyst (with magnet) has a ~ 1.7 times higher current density than the catalyst (without magnet). Overpotential is decreased by 114 mV at 5 mA cm^{-2} for the catalyst when an external magnetic field is applied. In both cases, the chronoamperometry (CA) measurement was done at a constant potential of 2.0 V vs. Ag/AgCl for 40 min. Afterward, the electrolyte solution (4 mL) was taken into a polypropylene tube from the anodic chamber for H_2O_2 detection, and an o-tolidine solution (1 mL) was added to this electrolyte solution. This mixture was kept in the dark for 30 min, and subsequently, the absorbance of that solution was measured using a UV–visible spectrophotometer (Jasco V-730 spectrophotometer). The appearance of a peak at ~ 436 nm demonstrates the presence of hydrogen peroxide generated during the OER. However, from **Figure S5b**, it can be concluded that the H_2O_2 formation is significantly reduced when an external magnetic field is applied compared to the absence of an external magnetic field.

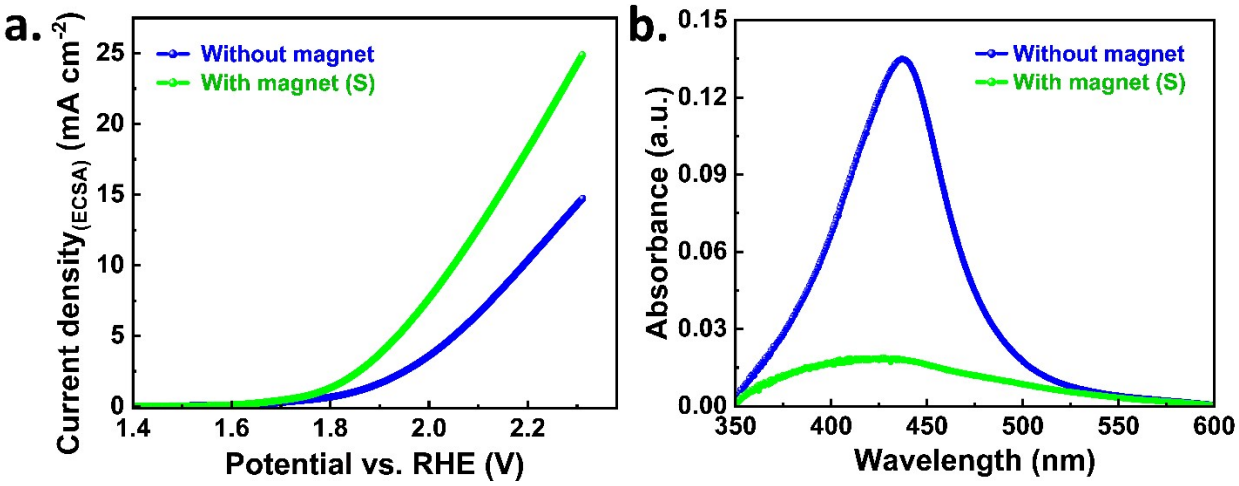

Figure S5. Estimation of hydrogen peroxide. (a) LSV plot of the catalyst (with and without magnet) in 0.1 M Na_2SO_4 electrolyte solution. (b) UV–visible absorption spectra (from the titration of 0.1 M Na_2SO_4 with an o-tolidine solution) for H_2O_2 detection.

Current density vs. applied potential showing three independent measurements for each type of electrode:

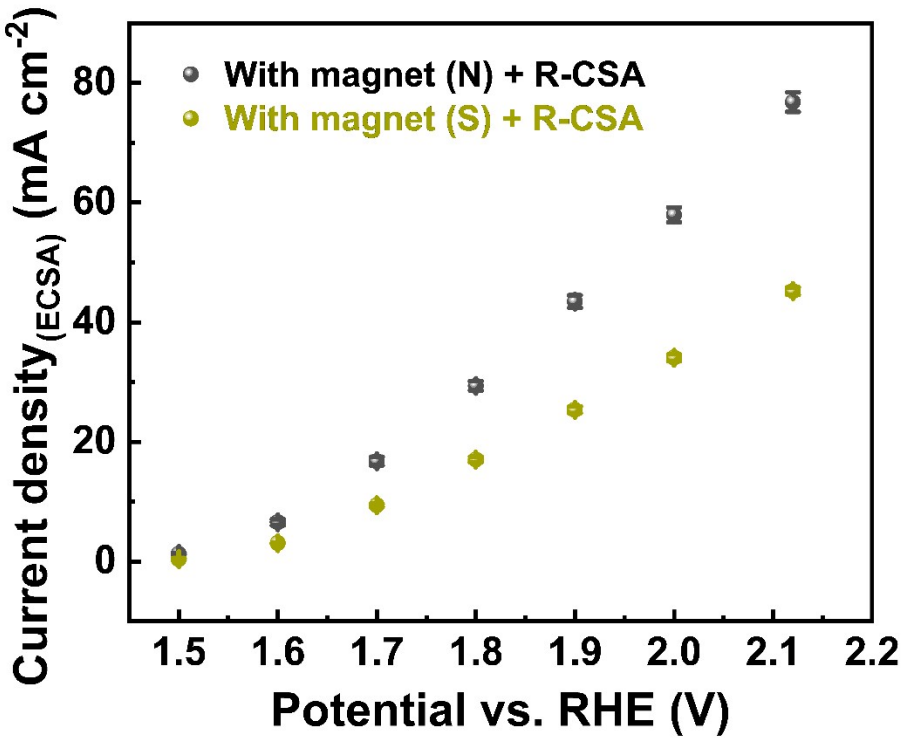

Figure S6. Current density vs. applied potential in the form of an error bar in 1 M KOH at a scan rate of 5 mV s^{-1}. Current density is normalized with electrochemically active surface area (ECSA).

Double-layer capacitance (C_{dl}):

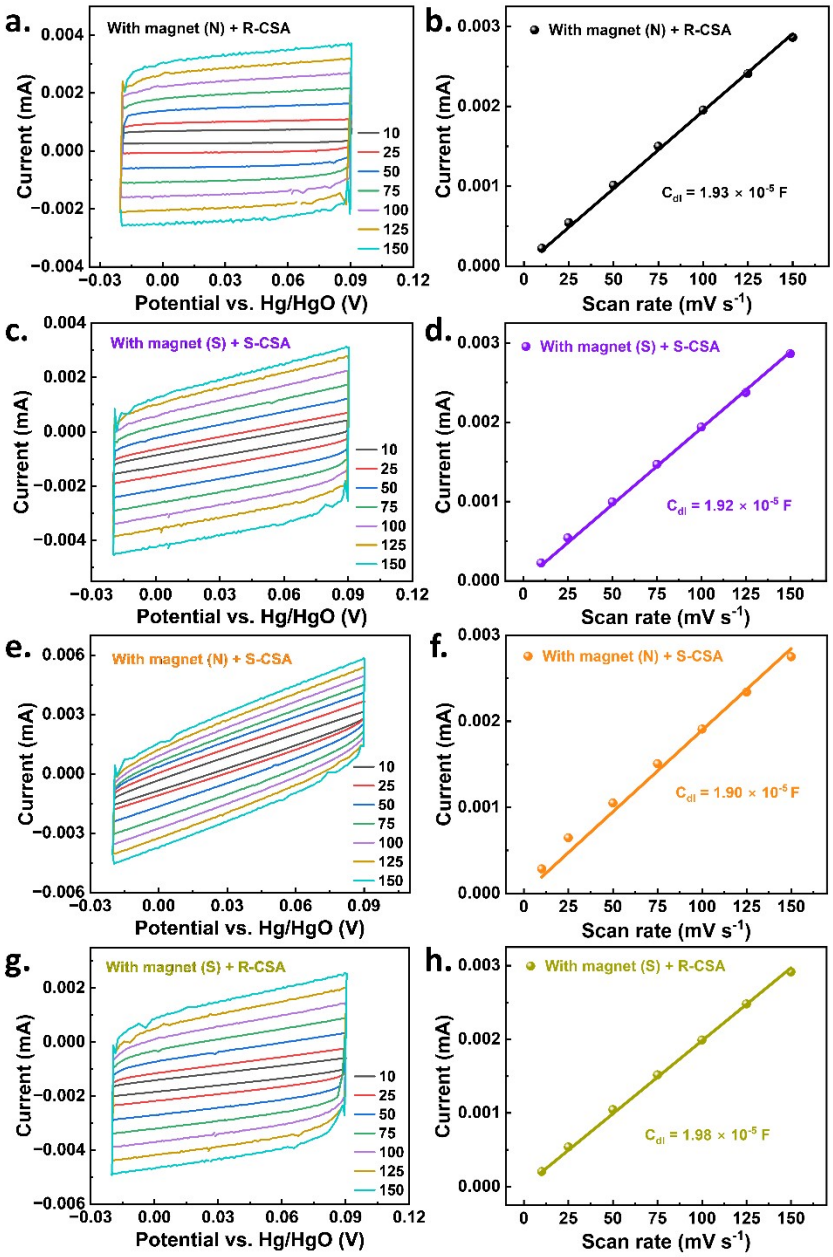

Figure S7. CV plots with different scan rates (10–150 mV s^{-1}) and plots of the average current at 0 V (vs. Hg/HgO) vs. scan rates of (a, b) with magnet (N) + R-CSA, (c, d) with magnet (S) + S-CSA, (e, f) with magnet (N) + S-CSA, and (g, h) with magnet (S) + R-CSA.

Error bar for electrochemical active surface area (ECSA):

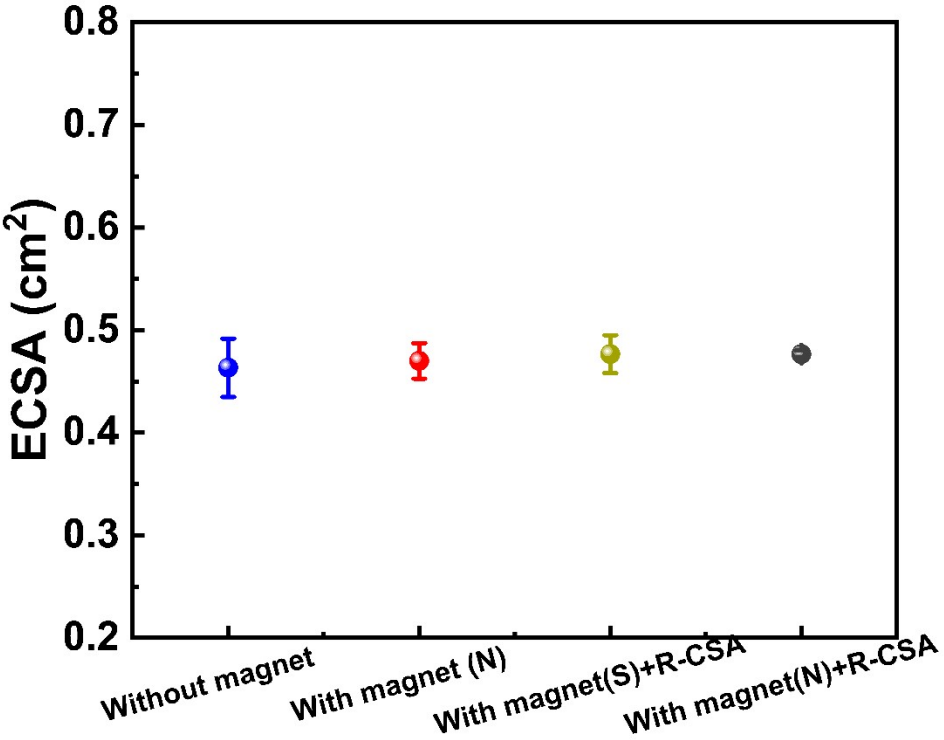

Figure S8. ECSA for all type of electrode in the form of error bar.

Characterizations of only catalyst and the catalyst modified with the chiral molecule on the FTO substrate:

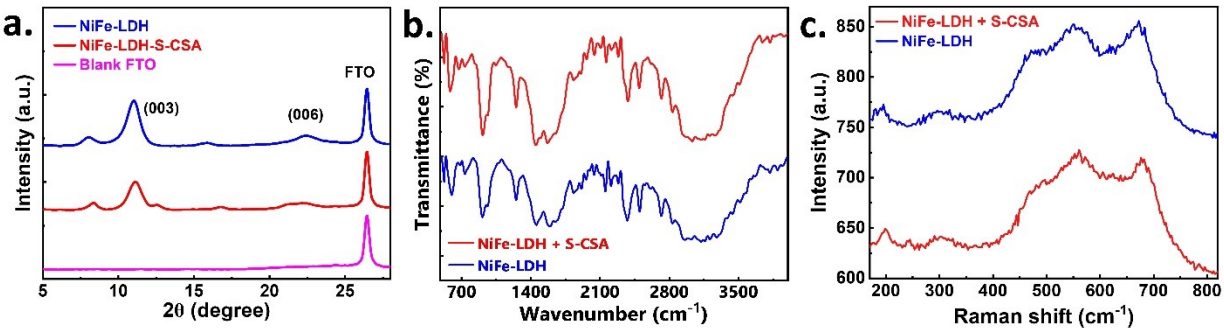

Figure S9. (a) XRD (b) FT-IR and (c) Raman spectra of only the catalyst and the catalyst modified with the chiral molecule on the FTO substrate.

Stability plot:

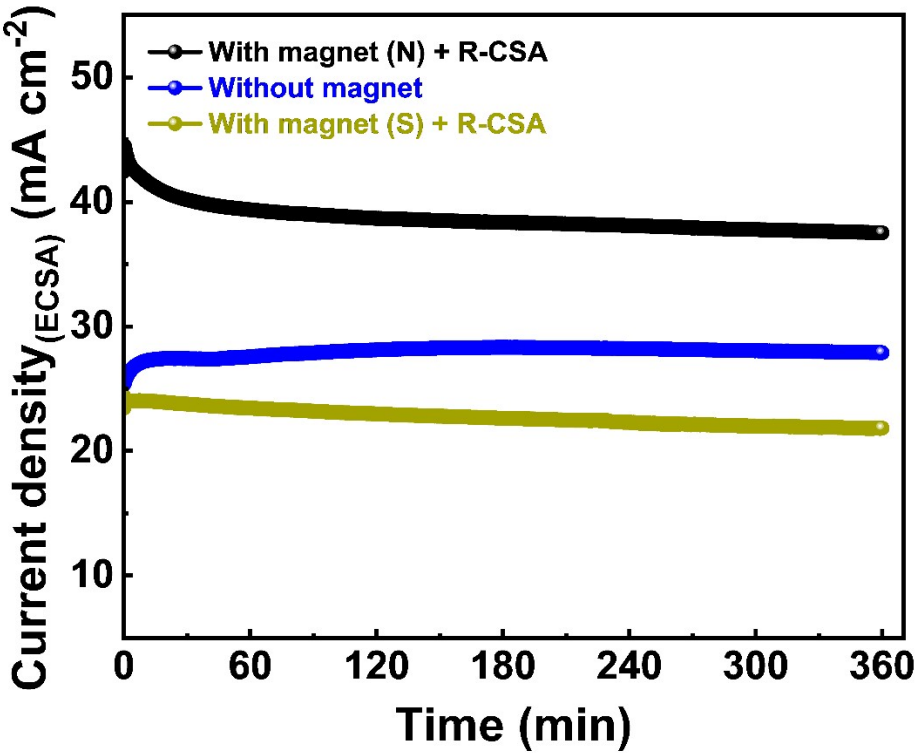

Figure S10. Chronoamperometry (CA) measurement done in a 1 M KOH for 6 h at a constant potential of 1 V vs. Hg/HgO to check the stability of catalyst.

LSV plot of the catalyst under different magnetic field:

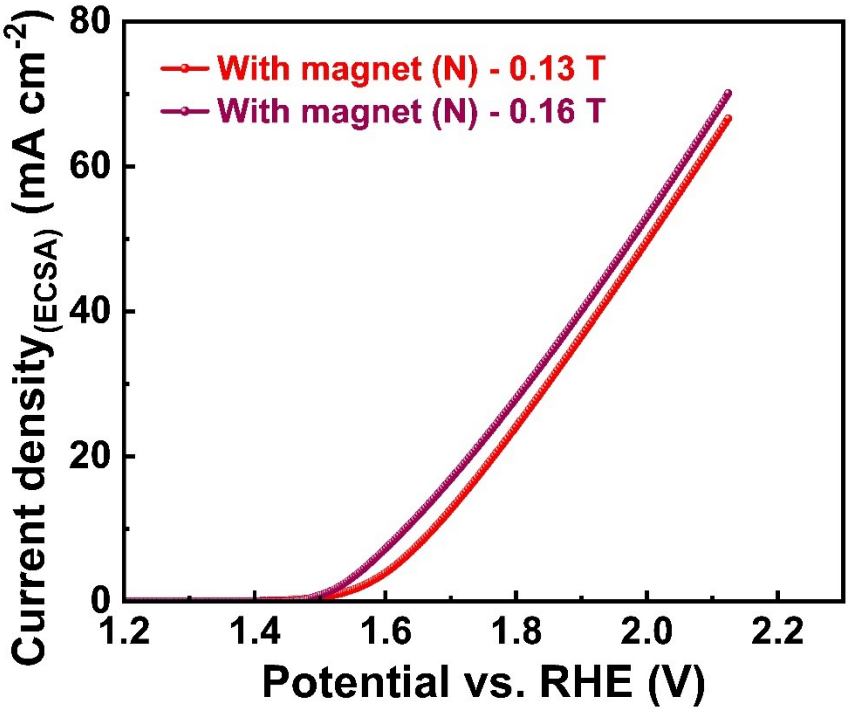

Figure S11. LSV plot of the catalyst in the presence of an external magnetic field (0.13 T and 0.16 T) in 1 M KOH at a scan rate of 5 mV s^{-1}.

Linear sweep voltammetry (LSV) plot of chirally modified catalyst without magnetic field:

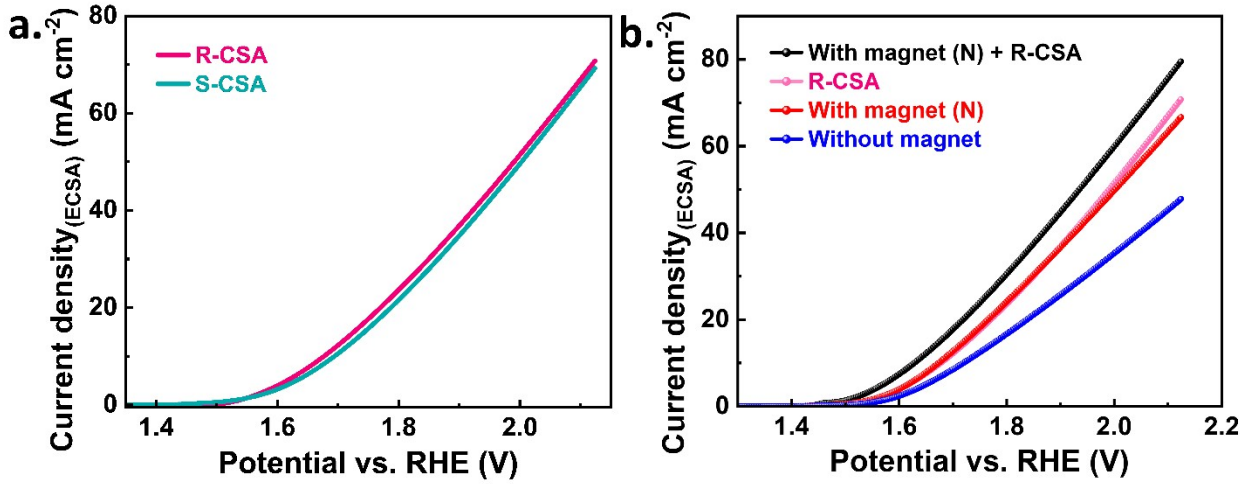

Figure S12. Current density vs. applied potential in 1 M KOH at a scan rate of 5 mV s^{-1}. (a) LSV plot of the catalyst modified with only the chiral molecule. (b) Comparison plot of different electrodes. Current density is normalized with electrochemically active surface area (ECSA).

Post OER characterization:

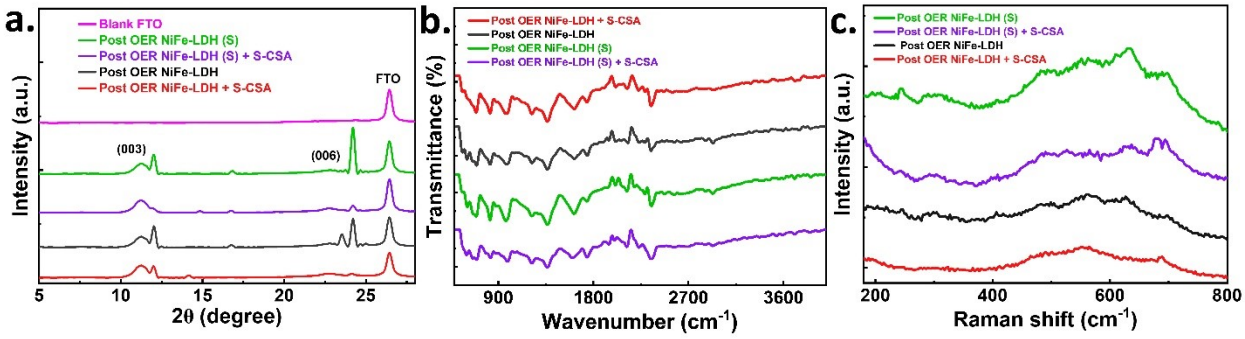

Figure S13. Post OER characterization after 6 h chronoamperometry test in 1 M KOH (a) XRD, (b) FT-IR, and (c) Raman spectra.

Table S1: Comparison of overpotential and Tafel slope parameters to those reported by others and this electrocatalyst material:

Catalyst	Spin Polarisation effects	Substrate	Overpotential (mV)	Tafel slope (mV dec^{-1})	Reference
Chiral tartrate-intercalated NiFe LDH (*L*-/*D*-Tar-LDH)	CISS effect	Nickel Foam	160 @10 mA cm^{-2}	41.8	[7]
NiFe-LDHs	Magnetic field	Carbon Paper	246 @10 mA cm^{-2}	108.3	[8]
NiFe LDH	Magnetic field	Rotating Disk Electrode	207 @10 mA cm^{-2}	41.7	[9]
Fe_3O_4@NiFe-LDH	Magnetic core	Carbon	196 @30 mA cm^{-2}	102.2	[10]
NiFe-LDH/Co_3O_4/NF	Magnetic field	Nickel Foam	274 @50 mA cm^{-2}	81	[11]
NiFe LDH	-	Nickel Foam	249 @50 mA cm^{-2}	54	[12]
NiFe LDH	-	Glassy carbon disk electrode	347 @10 mA cm^{-2}	67	[1]
NiFe-LDH (S) +S-CSA	Magnetic field + CISS effect	FTO	400 @10 mA cm^{-2}	107	**This Work**

Table S2: Comparison of overpotential and Tafel slope parameters of different types of materials:

Catalyst	Electrolyte	Substrate	Overpotential (mV)	Tafel slope (mV dec^{-1})	Reference
Co_3O_4	1 M KOH	Au	400@10 mA cm^{-2}	49	[13]
Mn_3O_4	1 M KOH	GCE	>600@3 mA cm^{-2}	60	[14]
$NiFe_2O_4$	0.1 M KOH	GCE	440@10 mA cm^{-2}	98	[15]
NiCo-LDH	1 M KOH	GCE	335@10 mA cm^{-2}	41	[1]
CoCo LDH	1 M KOH	GCE	350@10 mA cm^{-2}	45	[1]
FeNi-rGO LDH	1 M KOH	Ni foam	195@10 mA cm^{-2}	39	[16]
$Ni(OH)_2$	0.1 M KOH	Au	410@1 mA cm^{-2}	-	[17]
$CoFe_2O_4$	1 M KOH	Glassy carbon	-	82.8	[18]
$NiZnFe_4O_x$	1 M KOH	Ni	425@100 mA cm^{-2}	-	[19]
NiCoFe-MOF-74	1 M KOH	Carbon paper	273@10 mA cm^{-2}	63	[20]

Reference

1 F. Song and X. Hu, *Nat Commun*, 2014, **5**, 4477.
2 S. R. Jena and J. Choudhury, *Chem. Commun.*, 2020, **56**, 559–562.
3 T. Plett, M. L. Thai, J. Cai, I. Vlassiouk, R. M. Penner and Z. S. Siwy, *Nanoscale*, 2017, **9**, 16232–16243.
4 H.-J. Rhoo, H.-T. Kim, J.-K. Park and T.-S. Hwang, *Electrochimica Acta*, 1997, **42**, 1571–1579.
5 Ö. B. Mergen, E. Arda, S. Kara and Ö. Pekcan, *Polymer Composites*, 2019, **40**, 1862–1869.
6 P. Pal and A. Ghosh, *Journal of Applied Physics*, 2017, **122**, 015101.
7 J. H. Kim, H. Lee, Y. S. Park, J. Lee, J. Yun, S. Moon, S. Lee, C.-S. Jeong, J. Lee, D. Kim, S.-J. Hwang, S. Kim and J. Moon, *Applied Catalysis B: Environment and Energy*, 2026, **385**, 126327.
8 L. Lin, R. Xin, M. Yuan, T. Wang, J. Li, Y. Xu, X. Xu, M. Li, Y. Du, J. Wang, S. Wang, F. Jiang, W. Wu, C. Lu, B. Huang, Z. Sun, J. Liu, J. He and G. Sun, *ACS Catal.*, 2023, **13**, 1431–1440.
9 X. Qin, J. Teng, W. Guo, L. Wang, S. Xiao, Q. Xu, Y. Min and J. Fan, *Catal Lett*, 2023, **153**, 673–681.
10 W. Cao, X.-H. Gao, J. Wu, A.-Q. Huang, H. Hu and Z.-W. Chen, *ACS Catal.*, 2024, **14**, 3640–3646.
11 Y. Zhang, P. Guo, S. Niu, J. Wu, W. Wang, B. Song, X. Wang, Z. Jiang and P. Xu, *Small Methods*, 2022, **6**, 2200084.
12 S. Liu, H. Zhang, E. Hu, T. Zhu, C. Zhou, Y. Huang, M. Ling, X. Gao and Z. Lin, *J. Mater. Chem. A*, 2021, **9**, 23697–23702.
13 J. A. Koza, Z. He, A. S. Miller and J. A. Switzer, *Chem. Mater.*, 2012, **24**, 3567–3573.
14 S. Hirai, S. Yagi, A. Seno, M. Fujioka, T. Ohno and T. Matsuda, *RSC Adv.*, 2016, **6**, 2019–2023.
15 M. S. Al-Hoshan, J. P. Singh, A. M. Al-Mayouf, A. A. Al-Suhybani and M. N. Shaddad, *International Journal of Electrochemical Science*, 2012, **7**, 4959–4973.
16 X. Long, J. Li, S. Xiao, K. Yan, Z. Wang, H. Chen and S. Yang, *Angew Chem Int Ed*, 2014, **53**, 7584–7588.
17 O. Diaz-Morales, I. Ledezma-Yanez, M. T. M. Koper and F. Calle-Vallejo, *ACS Catal.*, 2015, **5**, 5380–5387.
18 X. Ren, T. Wu, Y. Sun, Y. Li, G. Xian, X. Liu, C. Shen, J. Gracia, H.-J. Gao, H. Yang and Z. J. Xu, *Nat Commun*, 2021, **12**, 2608.
19 F. A. Garcés-Pineda, M. Blasco-Ahicart, D. Nieto-Castro, N. López and J. R. Galán-Mascarós, *Nat Energy*, 2019, **4**, 519–525.
20 H. Zheng, Y. Wang, P. Zhang, F. Ma, P. Gao, W. Guo, H. Qin, X. Liu and H. Xiao, *Chemical Engineering Journal*, 2021, **426**, 130785.